

Dynamics of moored arctic spar interacting with drifting level ice using discrete element method

HaKun Jang^{*1} and MooHyun Kim²

¹LSU Center for Computation and Technology, Louisiana, 340 E Parker Blvd, Baton Rouge, LA 70808, USA

²Department of Ocean Engineering, Texas A&M University,
727 Ross Street, College Station, Texas 77843, USA

(Received September 20, 2021, Revised October 10, 2021, Accepted October 12, 2021)

Abstract. In this study, the dynamic interaction between an Arctic Spar and drifting level ice is examined in time domain using the newly developed ice-hull-mooring coupled dynamics program. The in-house program, CHARM3D, which is the hull-riser-mooring coupled dynamic simulator is extended by coupling with the open-source discrete element method (DEM) simulator, LIGGGHTS. In the LIGGGHTS module, the parallel-bonding method is implemented to model the level ice using an assembly of multiple bonded spherical particles. As a case study, a spread-moored Arctic Spar platform, whose hull surface near waterline is the inverted conical shape, is chosen. To determine the breaking-related DEM parameter (the critical bonding strength), the four-point numerical bending test is used. A series of numerical simulations is systematically performed under the various ice conditions including ice drift velocity, flexural strength, and thickness. Then, the effects of these parameters on the ice force, platform motions, and mooring tensions are discussed. The simulations reveal various features of dynamic interactions between the drifting ice and moored platform for various ice conditions including the novel synchronous resonance at low ice speed. The newly developed simulator is promising and can repeatedly be used for the future design and analysis including ice-floater-mooring coupled dynamics.

Keywords: arctic spar; DEM simulation; ice-floater-mooring dynamics; level ice; parametric study; parallel bonding method; synchronous resonance

1. Introduction

Level ice is floating ice characterized with unaffected surface by deformation. When it hits the sloped structure, the most dominant failure mode of level ice is bending. Due to the complexity of ice material as well as the interaction with the structure, from mid-60's, extensive efforts have been made to estimate the ice impact on the sloped structure. Lavoie (1966) first introduced the theoretical derivation for ice breaking force on the conical structure based on the plate on elastic foundation theory. Croasdale (1980,1994), Mayne (2007), and Lu *et al.* (2014a) further developed this derivation by adding 3D effects and other force contributions such as rubble accumulation, turning ice force, pushing force, and so on. Ralston (1980) also formulated the ice-force equation based on the plastic limit analysis considering ride up and breaking forces. These two main approaches are

*Corresponding author, Post-doctoral researcher, E-mail: hjang3@lsu.edu

adopted in the international standard, ISO 19906 (2010).

However, there are still gaps between theoretical calculation of ice force and field-measurement/model-test data. For example, despite field- and model-test data reveal that the ice drift velocity plays a significant role in the period of ice force (Yan *et al.* 2006, Yue *et al.* 2007, Tian and Huang 2013), it is not a parameter in those two theoretical equations. In addition, those two approaches were formulated for the fixed structures rather than compliant or moored structures, for which coupled-dynamic interactions should be considered. Although various numerical methods were also applied to investigate the interaction between level ice and sloped fixed structures (Cohesive Element Method in Lu *et al.* (2014b) and Wang *et al.* (2018); Finite Element Method in Paavilainen *et al.* (2011), and Jeon and Kim (2021); Discrete Element Method in Ji *et al.* (2015), Di *et al.* (2017), and Jou *et al.* (2019)), level ice interacting with moored floating structures has not been seriously studied yet.

In this paper, a numerical simulation program is developed to examine the three-dimensional coupled dynamics between level ice and moored Arctic Spar in time domain. The DEM with parallel bonding model is used to model the level ice, and 6-DOF rigid-body motions of Arctic Spar and fourteen-mooring-line dynamics are solved simultaneously in a combined matrix at each timestep. In Jang and Kim (2021a, b), the results from the time-domain simulations were compared reasonably with experimental results for a fixed structure (Barker *et al.* 2005, Gravesen *et al.* 2005) and shallow-draft floater (Nixon and Etema 1988). Here, a series of numerical simulations for a deep-draft spread-moored arctic spar are performed for various ice conditions (drift velocity, ice thickness, ice bending stiffness) and the resulting ice forces, structural motions, and mooring tensions are discussed.

Rest of the article is organized as follows. In section 2, a brief overview of the coupling algorithm between in-house hull-mooring coupled dynamics program, CHARM3D, and open-source DEM simulator, LIGGGHTS, is described. The governing equation of Arctic Spar considering the mooring and hydrodynamic effects are presented in Section 2.1. and the details of the DEM are discussed in Section 2.2. The numerical simulation setup for the DEM and geometrical definition of Arctic Spar and mooring lines are described in section 3. The main results of this study are presented and discussed in section 4, where this promising simulator can capture the main features of dynamic interactions between level ice and moored Arctic Spar. Section 5 presents the conclusions and remarks for future directions.

2. Numerical method

The newly developed numerical simulator is achieved by coupling two existing programs, CHARM3D and LIGGGHTS (Kloss *et al.* 2012). The in-house program, CHARM3D, developed by the second author's research group is a coupled-floater-mooring solver in time-domain, considering the hydrodynamic effects on a floater and mooring lines. LIGGGHTS which is the open-source program, is the time-domain simulator for granular materials based on the discrete element method.

CHARM3D and LIGGGHTS have different programming approaches. First, CHARM3D and LIGGGHTS use different computational languages: Fortran77 vs. C++. Second, the programming methods are different: procedural programming (PP) vs. object-oriented programming (OOP). Thus, implementing one program with another requires considerable work. Therefore, the external coupling method is used for this study. The two programs run individually, but by sharing the data

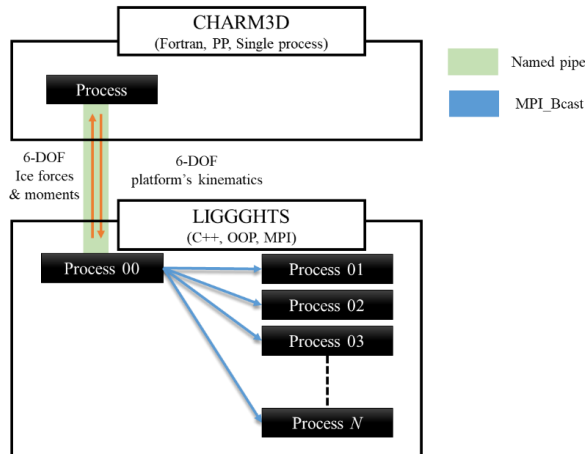


Fig. 1 Diagram for external coupling between CHARM3D and LIGGGHTS (Jang and Kim 2021b)

externally through the computer memory system, they feed and obtain the necessary data from/to each other.

The external coupling between the two programs is achieved using a named pipe method, which links two separate processes. Each process can access a file system in Unix in the first-in-first-out (FIFO) manner to transfer/receive the data to the other. If one process interacts with the named pipe system, none of the processes should wait for it to complete its work and available to transfer/receive data after that. Because the named pipe provides the function of a data buffer, if two program have the same simulation timestep, a time-marching algorithm is not necessary for coupling.

Another coupling issue is MPI coding in LIGGGHTS. MPI stands for message passing interface, which allows the parallel computation of simulations with multiple processes. The primarily process moves data to another process to distribute the computation load, and the simulation runs in parallel. It is useful to simulate multiple particles by reducing the computation time efficiently. In LIGGGHTS, the primary process (rank 0) receives the platform’s kinematics data from CHARM3D and distributes this information to other processes by using the call function, “MPI_Bcast.” This communication occurs after the first integration step when the particle positions have been updated. The general schemes of communication between multiple processes are depicted in Fig. 1. CHARM3D provides 6-DOF platform’s kinematics to LIGGGHTS, and LIGGGHTS feeds 6-DOF ice forces and moments into CHARM3D.

2.1 Floater and mooring dynamics in CHARM3D

CHARM3D solves the 6-DOF floater’s motions with mooring lines based on Eq. (1) below.

$$[M + M_{add}(\infty)]\ddot{\zeta}(t) + K_{hydro}\dot{\zeta}(t) = F_{convolution}(t) + F_{nonlinear_drag}(t) + F_{mooring}(t) \quad (1)$$

where M and M_{add} is the mass and added mass of a floater, K_{hydro} is the hydrostatic stiffness, $F_{nonlinear_drag}$, $F_{convolution}$ and $F_{mooring}$ is the nonlinear drag, radiation damping and mooring force, respectively, and ζ is the 6-DOF floater’s motions. The added mass and radiation damping coefficients are evaluated/inpitted from a panel-based 3D diffraction and radiation program,

WAMIT (2006), in the frequency domain. The convolution force representing the memory effects of a free-surface fluid and nonlinear drag force based on Morison's equation are computed as follow

$$\begin{aligned} F_{convolution}(t, \zeta) &= - \int_{-\infty}^t b(\omega) \cos(\omega t) d\omega \\ F_{nonlinear_drag}(t) &= \frac{1}{2} \rho_w C_d A \dot{\zeta} |\dot{\zeta}| \end{aligned} \quad (2)$$

where ρ_w is the water density, C_d is the drag coefficient, A represents and projected area, and $b(\omega)$ is the linear radiation damping matrix at frequency, ω .

2.2 Level ice dynamics in LIGGGHTS

LIGGGHTS solves the dynamics of granular particles and tracks the motions of each particle based on Newton's Second Law of motion.

$$m_p \frac{du_p}{dt} = F_c + F_g + F_b + F_d \quad (3)$$

where m_p , u_p , I_p , and ω_p are the mass, translational velocity, moment of inertia, and angular velocity of the particle, respectively, and F_c , F_g , F_b , and F_d are the contact, gravitational, buoyancy, and drag forces, respectively.

2.2.1 Contact model for particles

The normal and tangential contact forces for particle-particle and particle-wall interaction are calculated based on the Hertz-Mindlin nonlinear model as follow

$$\begin{aligned} F_c &= F_n + F_t \\ F_n &= -k_n \delta_n - \gamma_n v_n \\ F_t &= \begin{cases} -k_t \delta_t - \gamma_t v_t, & |F_t| \leq \mu_s |F_n| \\ -\mu_s |F_n|, & |F_t| > \mu_s |F_n| \end{cases} \end{aligned} \quad (4)$$

where n and t denote the normal and tangential components, respectively, k is the stiffness, γ is the damping constant, v is the relative velocity between the two particles, δ_n is the overlap of outer particles surfaces, and δ_t is the tangential displacement used in a frictional yield criterion. The coefficients used in the contact force calculation are defined by material's physical properties such as the mass (m), radius (R), Young's modulus (E), Shear modulus (G), Poisson ratio (ν), and restitution coefficient (e).

$$\begin{aligned} k_n &= \frac{4}{3} Y^* \sqrt{R^* \delta_n}, \\ \gamma_n &= -2 \sqrt{\frac{5}{6}} \beta \sqrt{S_n m^*} \geq 0, \\ k_t &= 8G^* \sqrt{R^* \delta_n}, \\ \gamma_t &= -2 \sqrt{\frac{5}{6}} \beta \sqrt{S_t m^*} \geq 0 \end{aligned} \quad (5)$$

$$\begin{aligned}
 S_n &= 2Y^* \sqrt{R^* \delta_n}, \quad S_t = 8G^* \sqrt{R^* \delta_n}, \\
 \beta &= \frac{\ln(e)}{\sqrt{\ln^2(e) + \pi^2}}, \quad \frac{1}{Y^*} = \frac{(1-\nu_i^2)}{Y_i} + \frac{(1-\nu_j^2)}{Y_j} \\
 \frac{1}{G^*} &= \frac{2(2-\nu_i)(1+\nu_i)}{Y_i} + \frac{2(2-\nu_j)(1+\nu_j)}{Y_j} \\
 \frac{1}{R^*} &= \frac{1}{R_i} + \frac{1}{R_j}, \quad \frac{1}{m^*} = \frac{1}{m_i} + \frac{1}{m_j}
 \end{aligned}$$

2.2.2 Parallel bonding method

In order to mimic the realistic fracture of level ice, the parallel bonding method is employed in LIGGGHTS, which is firstly introduced by Potyondy and Cundall (2004). The particles are initially linked together and transfer interaction forces through the bonding disk as depicted in Fig. 2. By calculating the elastic deformation of the bonding disk, the interaction forces and moments including tension, compression, shear, twisting, and bending moment can be computed as follow

$$\begin{cases} F_b = F_{nb}n_i + F_{tb}t_i = k^{nb}U^n + k^{tb}U^t \\ M_b = M_{nb}n_i + M_{tb}t_i = k^{tb}J\theta^n + k^{nb}I\theta^t \end{cases} \quad (6)$$

$$\begin{cases} I = \frac{1}{4}\pi R^4, \quad J = \frac{1}{2}\pi R^4 \\ k^{nb} = \frac{E}{D}, \quad k^{tb} = \frac{G}{D} = \frac{E}{2(1+\nu)} \frac{1}{D} \end{cases}$$

where n and t denote the normal and tangential direction vectors, F_b and M_b are the bonding forces and moments on the bonding disk, I and J are the moment of inertia and polar moment of inertia of the parallel bond cross-section, and k , U , and θ represent the stiffness coefficients, transverse displacements, and rotational displacements, respectively. The normal and tangential bonding stiffness in Eq. (6) are determined by the function of the elastic modulus (E), Poisson's ratio (ν), and particle diameter (D) based on Potyondy and Cundall (2004).

Once the internal stress (σ_b or τ_b) in the bonding disk exceeds the prescribed critical bonding stress ($\sigma_{b \max}$ or $\tau_{b \max}$), the link between particles breaks, and the particles behave as an individual particle. Therefore, the contact force is computed based on Eq. (4) instead of Eq. (6). The failure criteria complying with the beam theory are given by

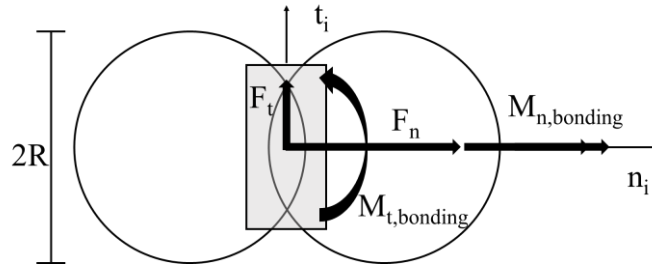


Fig. 2 Schematic view of parallel bonding method (Jang and Kim 2021b)

$$\begin{aligned}\sigma_b &= \frac{|F_{nb}|}{A} + \frac{|M_{tb}|R}{I} < \sigma_{b \max} \\ \tau_b &= \frac{|F_{tb}|}{A} + \frac{|M_{nb}|R}{J} < \tau_{b \max}\end{aligned}\quad (7)$$

3. Numerical simulation setup

In the current study, we directly adopt the same floater model used in Jang *et al.* (2016) with the same level ice condition for comparison.

3.1 Ice properties in DEM simulations

In DEM model, the parallel bonding method requires the prescribed artificial parameters, the maximum bonding stress ($\sigma_{b \max}$ or $\tau_{b \max}$), to mimic the bonding relations between particles. To determine this maximum bonding stress, the numerical four-point beam tests are systematically conducted. The three-layered beam whose cross-section size is $b \times h = 2.73\text{m} \times 2\text{m}$ is modeled with total 258 particles as depicted in Fig. 3. The hexagonal closed-packing (HCP) pattern is used for the ice block geometry, resulting in the particle's diameter of 0.76 m, complying with the Eq. (8). Table 1 summarize the parameters used in the DEM simulations.

$$D = \frac{h}{(1+(w-1)\sqrt{2/3})}\quad (8)$$

The two loading pins on the middle gradually push the beam upward with the constant velocity of 0.001 m/s, and the forces on two loading pins are measured in time. These forces are averaged and transformed to the stress based on the elastic beam theory in Eq. (9). The parametric studies are conducted by varying the maximum bonding stress ($\sigma_{b \max}$ or $\tau_{b \max}$), and determined them when the maximum stress is coincide with the given flexural stress. The detailed procedure of the four-point numerical bending test is discussed in Jang and Kim (2021a).

$$\sigma_{flexural} = \frac{3F(L-L_i)}{2bh^2}\quad (9)$$

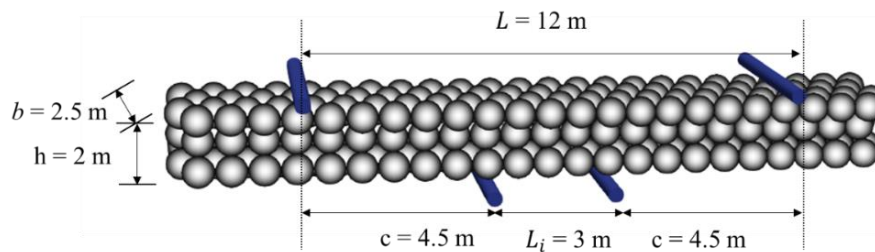


Fig. 3 Dimension of four-point numerical beam bending tests

Table 1 Ice properties of level ice

Parameter	Symbol	Unit	Value
Ice thickness	h_i	m	2
Particle diameter	D	m	0.76
Poisson's ratio	ν	-	0.3
Young's Modulus	E	GPa	4
Flexural Strength	σ_f	kPa	500
Frication coefficient (ice-ice)	μ_{ii}	-	0.3
Frication coefficient (ice-structure)	μ_{is}	-	0.3
Restitution coefficient	e_{ii}	-	0.1
Ice density	ρ_i	kg/m ³	900
Water density	ρ_w	kg/m ³	1025

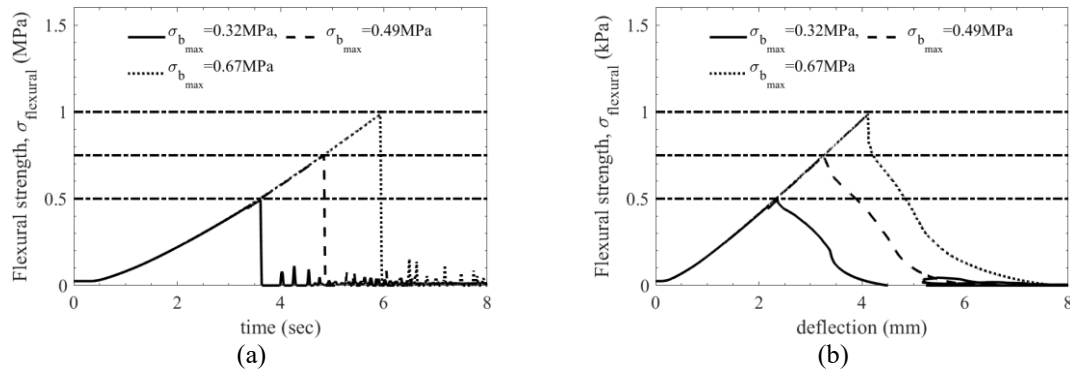


Fig. 4 (a) Time-flexural strength curve and (b) time-deflection curve

Fig. 4 show the time history of the flexural stress at the middle of the beam. In the current study, since the effects of bonding strength is also investigated, three reference lines of targeted flexural strengths are plotted in the same figure. As a results, to achieve the targeted flexural strengths of 0.5, 0.75, and 1 Mpa, the corresponding the maximum bonding stress of 0.32, 0.49, and 0.67 MPa shows the fits. From the deflection-stress curve and the slope, m , in the linear range, the elastic modulus of the beam is computed by Eq. (10), and the 3.4 GPa is obtained, which is comparable to the targeted elastic modulus of 4 GPa. With this numerical validation, the maximum bonding strength determined by the numerical beam-bending test is used the further numerical simulations hereafter.

$$E = \frac{\sigma_{flexural}(3L^2 - 4c^2)}{12hm} \quad (10)$$

3.2 Actic Spar with mooring lines

The Arctic Spar with a 40-degree sloped angle is model in numerical simulations in LIGGGHTS and CHARM3D as depicted in Fig. 5. We directly adopted the structural properties for the platform and mooring lines summarized in Tables 1 and 2 in Jang *et al.* (2016). Only difference is the round

shape of Arctic Spar, whereas it is the squared shape in Jang *et al.* (2016). The fourteen catenary mooring lines are modeled with finite elements, and schematic view is depicted in Fig. 5(c). The natural periods and frequencies of Arctic Spar computed from the numerical free-decay tests are tabulated in Table 2. For efficiency of numerical simulations, the initial surge position of the structure is properly set so that the structural dynamic motion reaches the steady state earlier.

Table 2 Arctic Spar natural periods and frequencies

	Period (sec)	Frequency (rad/sec)
Surge	272.3	0.0231
Heave	24.7	0.2513
Pitch	39.0	0.1571

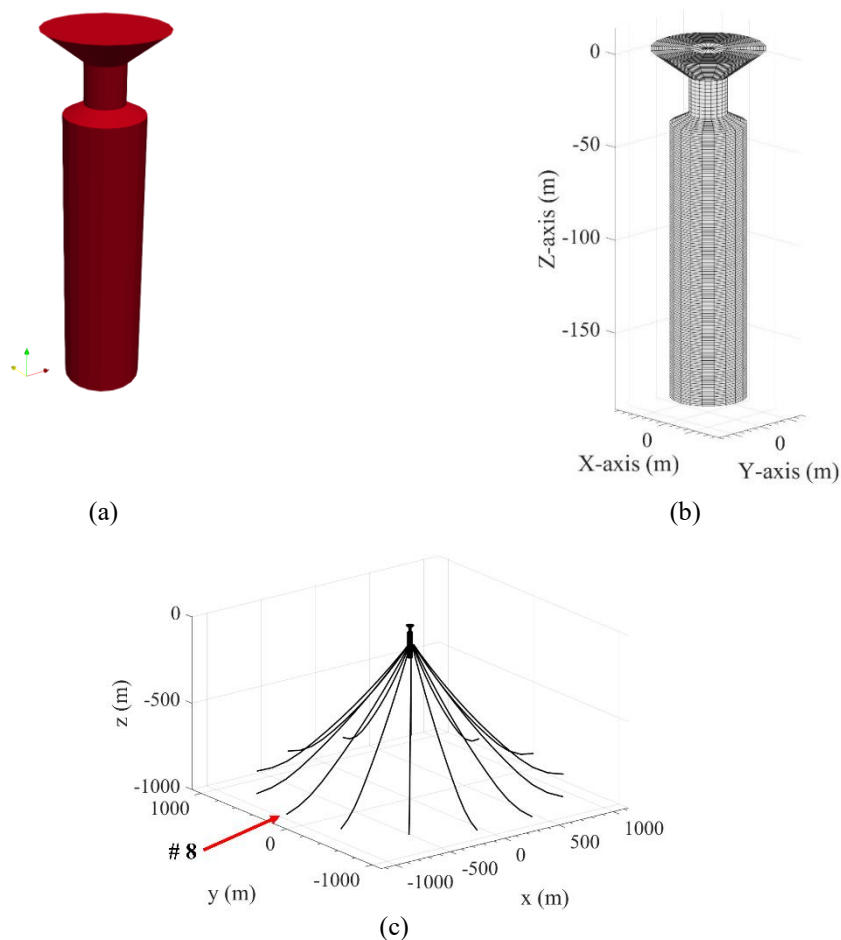


Fig. 5 Arctic Spar Model in (a) LIGGGHTS and (b) CHARM3D and (c) Mooring Configuration (the most critical taut-side mooring line #8 is indicated with an arrow)

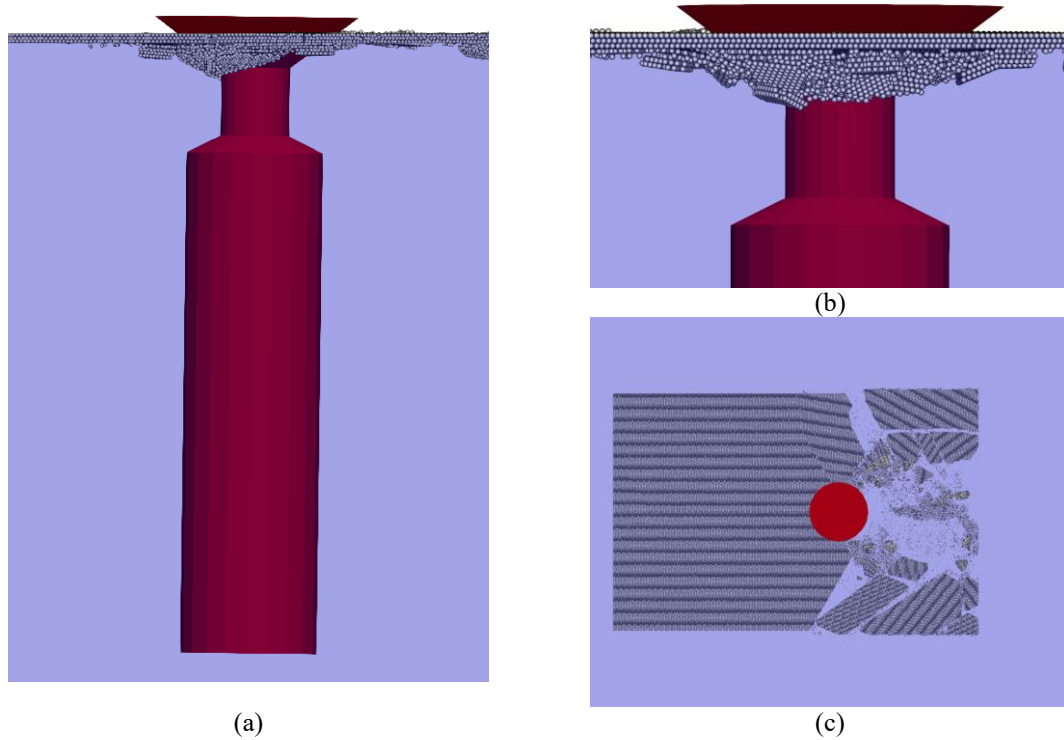


Fig. 6 Snapshots of the instantaneous ice-structure interaction at (a) side view, (b) front view, and (c) top view ($v_{ice} = 0.5$ m/s, $h_{ice} = 3$ m, and $\sigma_f = 0.75$ MPa)

4. Numerical results and discussions

In this section, a series of time-domain numerical simulations are conducted under various ice conditions and the corresponding numerical results are presented. As discussed in Section 2, 6-DOF platform motions, dynamics of 14 mooring lines, and its interaction with drifting level ice consisting of 0.6 M ~ 9.2 M spherical particles are considered in three-dimensional domain. We first discuss about the general features of level ice interaction with the arctic spar through visual observation. Subsequently, the influences of ice variables are discussed in more detail.

4.1 Visual observation and general features of interaction

Fig. 6 represents the dynamic interaction of an Arctic Spar with level ice. From the visual observation, the moving level ice generally fails in bending mode by either hitting the Arctic Spar or rubble ice under it. After considerable breaking, the broken ice pieces accumulate in front of the structure, as shown in Figs. 6(a) and 6(b). The large broken ice pieces are pushed away from the structure in the downstream as depicted in Fig. 6(c). The length of the accumulated rubble ice is approximately 3~5 times the ice thickness. These accumulated rubble ice pieces continuously push

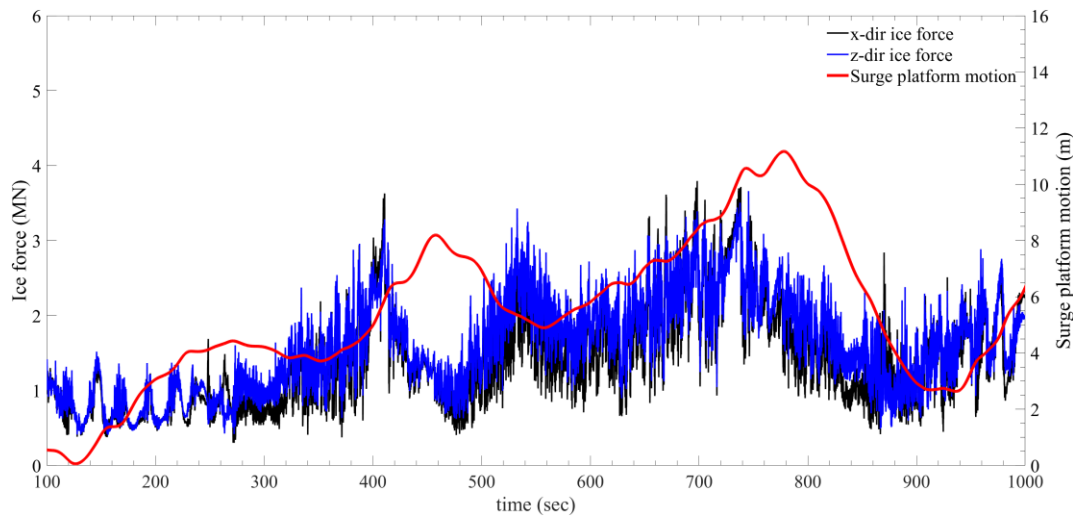


Fig. 7 Exemplary time-history of ice force in x- and z-direction, and surge platform motion ($v_{ice} = 0.1$ m/s, $h_{ice} = 2$ m, and $\sigma_f = 0.75$ MPa)

the structure until the structure gets back by mooring forces. The pattern is repeated showing oscillatory motions in surge. When level ice hits the structure, the radial cracks on intact ice are created at first, and the circumferential cracks are subsequently created, resulting in smaller broken ices, which is similar to the observations in previous literatures (Xu *et al.* 2015, Jang and Kim 2021b).

Fig. 7 shows exemplary time-histories of surge/heave ice forces and corresponding surge motions. The surge and heave ice forces show strong correlation by having the similar trend of time-series. Because of the large hull inclination angle of 40 degrees, the vertical ice force is as large as the horizontal ice force. In all cases, rubble pile-up around the sloped-conical surface is observed, and the ice forces have positive values over time. The positive mean horizontal ice force in the direction of level-ice drifting velocity is obvious. The positive mean vertical ice force results from the downward sliding of broken ice plate along the inclined hull surface causing lift-up force. If ice rubbles are accumulated below the inclined hull surface, they will also contribute to the positive vertical force. In the case of low ice speed, the rubble ices keep accumulated and pushes the structure continuously without being cleared. At the ice-drifting velocity of 0.1 m/s, the resonance of the spar in the surge direction is observed and the period of the ice force is close to the natural period of the slowly-varying large amplitude surge motion. When the x-directional ice force reaches the maximum, it pushes to increase the surge velocity. Then, the platform moves faster than the ice, so it is detached from the drifting level ice, which results in sudden ice-force reduction. Then, the structure moves back by mooring constrains while experiencing multiple collisions with the intact ice. Once the kinetic energy of the structure is dissipated and becomes zero, then the structure drifts again in the positive x direction with increased ice force.

By taking advantage of the 3D 6-DOF analysis, the exemplary time-series of the 6-DOF ice forces and platform motions are depicted in Fig. 8(a), where the ice drift velocity, thickness, and flexural strength are 0.1 m/s, 2 m, and 0.75 MPa, respectively. The exciting moments are measured with respected to the body origin which is (0, 0, 0) at rest. In the surge, heave, and pitch directions, positive forces/motions and positive mean values are recorded due to the pushing and lifting up of

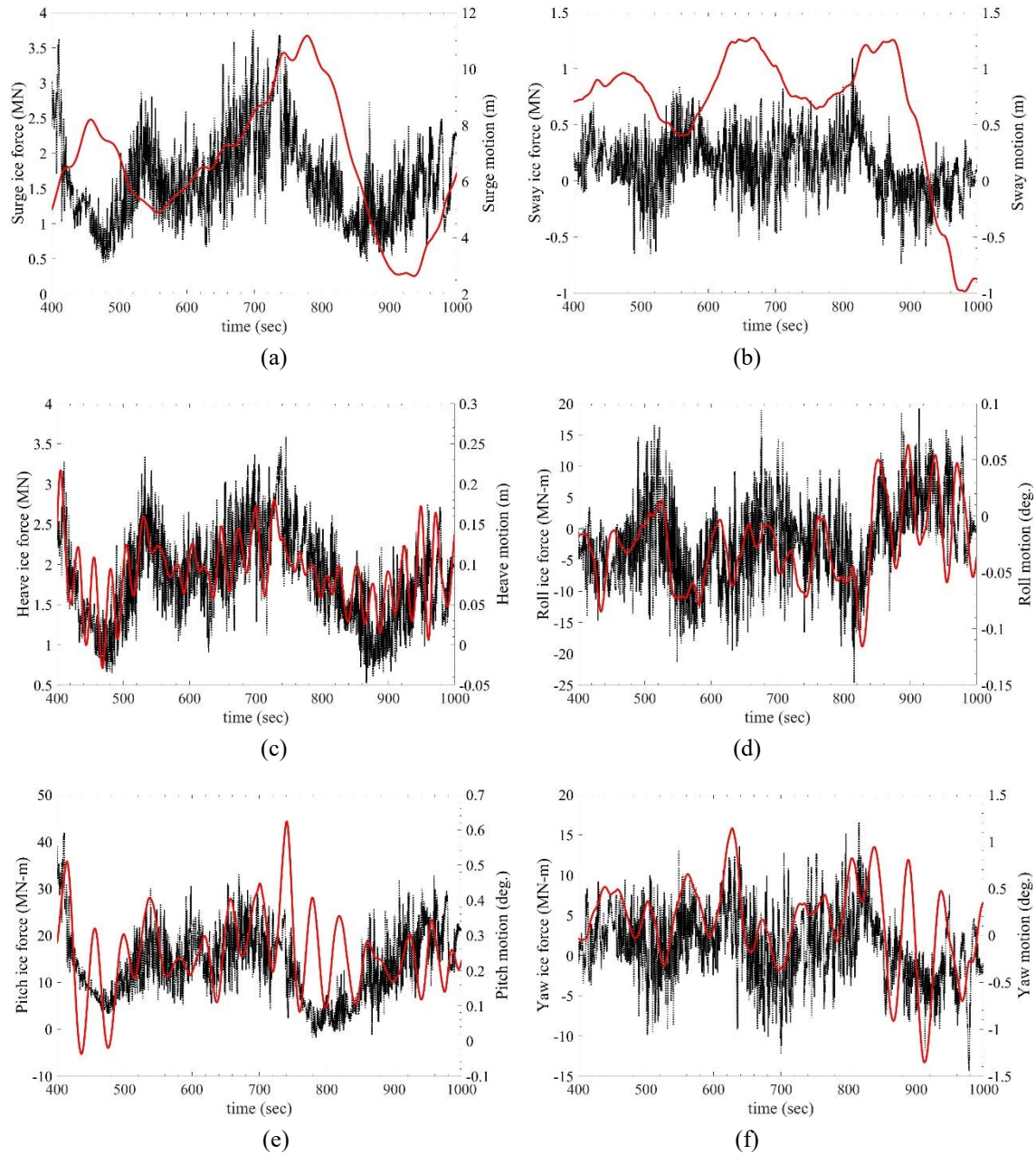


Fig. 8 (a) Time series of ice force and platform motion at (a) surge, (b) sway, (c) heave, (d) roll, (e) pitch, and (f) yaw directions (Black and red lines represent the ice force and platform motion, respectively; $v_{ice} = 0.1$ m/s, $h_{ice} = 2$ m, and $\sigma_f = 0.75$ MPa)

drifting and broken ice, as explained in the above. Although the ice moves in the x direction with constant speed, sway, roll, and yaw motions are observed because the broken pattern and the contact between the level ice and the structure takes place asymmetrically and non-simultaneously. Due to

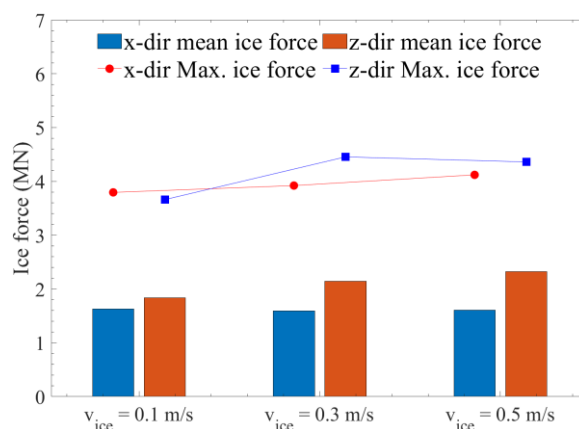


Fig. 9 Mean and Maximum ice force in x- and z-direction with varying ice velocity ($h_{ice} = 2$ m and $\sigma_f = 0.75$ MPa)

the eccentric forces on the structure, relatively large yaw motions occur in range of -1.5 to 1.5 degrees while smaller roll and pitch motions are observed. The mean values of sway, roll, and yaw motions are still close to zero due to the geometrical symmetry. All 6-DOF motions show the oscillatory behaviors with the dominant frequency equal to its own natural frequency, which is given in Table 2. The respective motions at their natural frequencies can be interpreted as continuous series of transient responses by ice-impact forces. Fig. 8(b) shows the same sets of 6-DOF ice forces and spar motions in the case of ice drift velocity=0.5 m/s, ice thickness=2 m, and ice flexural strength=0.75 MPa. The overall patterns of 6-DOF ice forces show the shift to higher frequencies compared to Fig. 8(a) in the random manner. All the 6-DOF motions occur at their own natural frequencies, similar to Fig. 8(a). However, at this higher ice drift velocity in Fig. 8(b), the patterns of heave and pitch motions do not tend to follow those of heave force and pitch moment, which is different compared to Fig. 8(a). With the increase in ice-drift velocity, the ice force frequency becomes closer to heave natural frequency, causing higher heave motions.

4.2 Effect of drift velocity

We investigate the influence of the ice drift velocity on the ice loads. Three ice drift velocities of 0.1 m/s, 0.3 m/s, and 0.5 m/s are chosen for ice thickness=2 m. Fig. 9 shows the comparison of mean and maximum ice forces in x- and z-direction with different velocities. Although both mean and maximum ice loads are slightly increased with increasing velocity, the difference is not significant, which is different from the case of fixed structure. According to Wang *et al.* (2018) and Jang and Kim (2021a), velocity effect is clearly demonstrated such that the ice load is 38% raised when the ice drift velocity is increased from 0.6 m/s to 1.8 m/s. Since Arctic Spar is more compliant with mooring lines, the momentum of level ice with drift velocity is more moderated by the movement of spar and thus the influence of ice speed on ice loads is less significant. This trend can be seen clearly when Fig. 8(a) is compared with Fig. 8(b).

In Fig. 10(a), the surge ice force spectra reveal that at $v_{ice} = 0.1$ m/s, the largest ice force energy is concentrated in the low frequency region, and the peak frequency is identical to the surge natural frequency of Arctic Spar as shown in Fig. 10(b). When ice drift velocity increases, ice force becomes

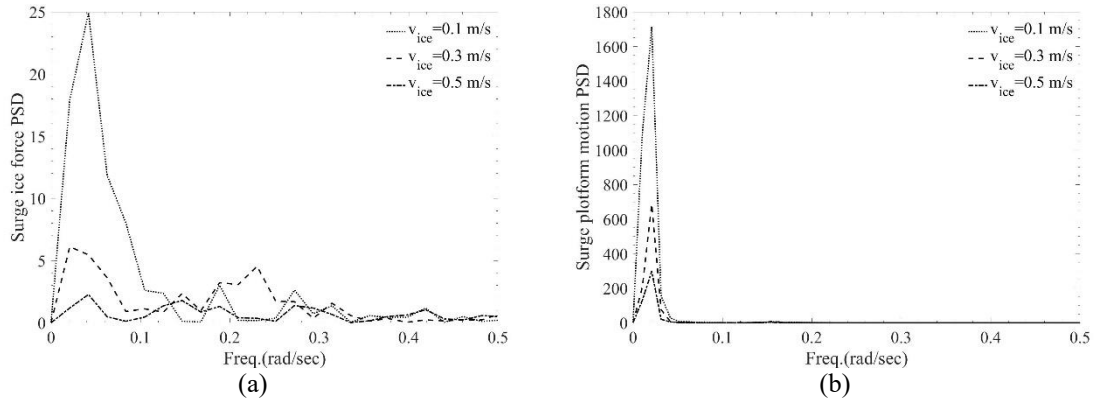


Fig. 10 Power spectral density of (a) surge ice load, and (b) surge platform motion ($h_{ice} = 2$ m and $\sigma_f = 0.75$ MPa)

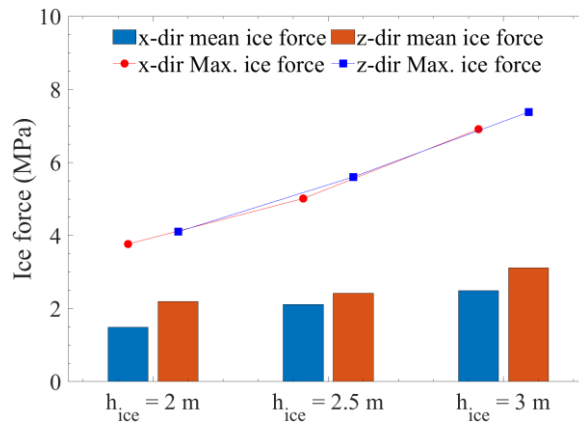


Fig. 11 Mean and Maximum ice force in x- and z-direction with varying ice thickness ($v_{ice} = 0.5$ m/s and $\sigma_f = 0.75$ MPa)

more random with less energy at low frequency, and more distributed over wider range of frequency, which results in smaller resonant surge motions. This trend can be clearly seen when we compare Figs. 8(a) and 8(b).

4.3 Effect of ice thickness

The effect of ice thickness is also investigated by varying the ice thickness. Three different ice thicknesses of 2 m, 2.5 m, and 3 m are considered. For this comparison, the flexural strength of ice is kept at 0.75 MPa, which means that the corresponding critical bonding strength for each thickness is adjusted to be 0.49 MPa, 0.45 MPa, and 0.43 MPa, respectively. The effect of varying flexural strength is also considered in the next section. To adjust the thickness with three layers, the diameter of spherical particles in the DEM is set to 0.759 m, 0.949 m, and 1.139 m for 2 m, 2.5 m, and 3 m ice thickness, respectively. Ice drift velocity of 0.5 m/s is applied for all three cases. Fig. 11 shows

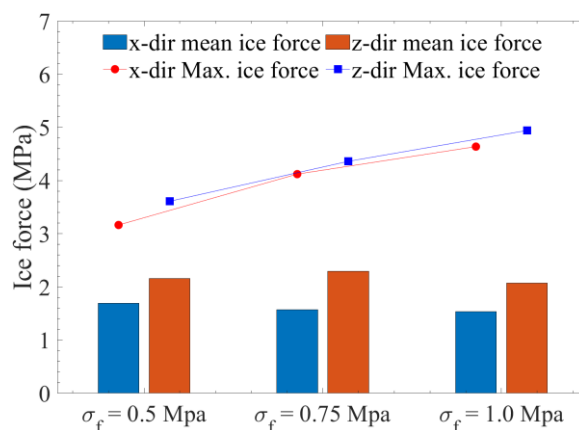


Fig. 12 Mean and Maximum ice force in x- and z-direction with varying ice thickness ($v_{ice} = 0.5$ m/s and $h_{ice} = 2$ m)

that both mean and maximum values of ice forces increase with increasing ice thickness, as can be intuitively expected. The thicker level ice possesses higher momentum which is transferred to the structure during collision process. The linear relation between ice momentum and mass(thickness) is similarly transferred to the linear relation between the ice load and ice thickness as shown in Fig. 11. Due to the increase in the mean ice forces, the mean surge offset of Arctic Spar is higher than the case of thin level ice.

4.4 Effect of flexural strength

Next, DEM simulations with three different ice flexural strengths, σ_f , of 0.5 MPa, 0.75 MPa, and 1 MPa are performed to investigate the influence of ice flexural strength. Numerical beam bending tests reveal that the critical bonding strengths corresponding to the above values are 0.32 MPa, 0.49 MPa, and 0.67 MPa, respectively. Fig. 12 shows the mean and maximum ice loads on the structure with varying ice flexural strength. The mean ice forces in x- and z-direction are not sensitive to varying ice flexural strength, while the maximum values are increased with increasing ice flexural strength. The maximum ice force of 4.6 MN at $\sigma_f = 1$ Mpa is about 50 % greater than 3.1 MN at $\sigma_f = 0.5$ Mpa. It is attributed to the increased ice-breaking force. Ice impact on the sloped structure typically consists of breaking, sliding, and accumulated forces (Aksnes 2010, Lu *et al.* 2014). The increasing flexural strength increases the breaking force, while other forces remain not much changed.

4.5 Mooring top tension

The mooring top tension of the most critical taut-side mooring line #8 in line with ice drift direction is presented in Fig. 13 and Table 3. In general, since the mooring tension is generally proportional to the platform surge motion, its pattern and statistical results have similar trend of those of the platform surge motion. With increasing ice drift velocity, the maximum surge motions decrease, as was observed in the previous figures, and thus mooring tensions also decrease. The largest surge motion and mooring tension at ice speed=0.1m/s were caused by the synchronous

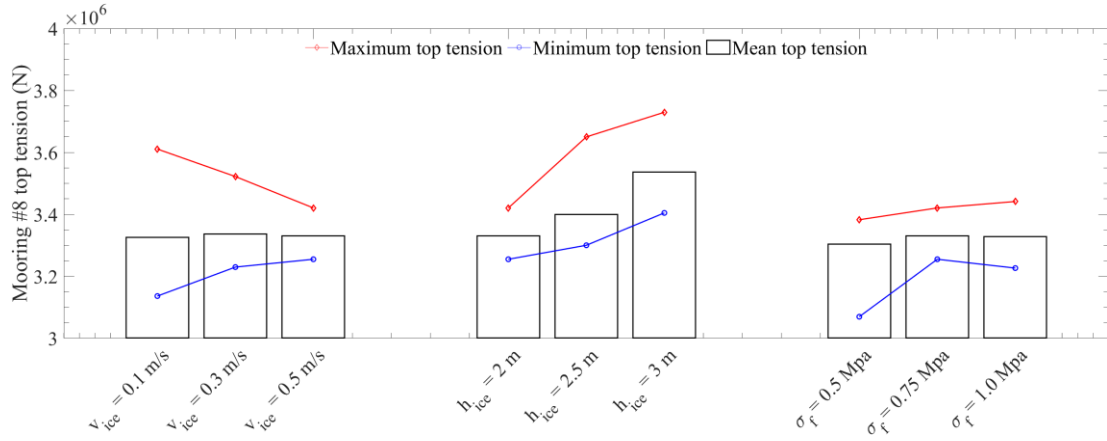


Fig. 13 Mooring top tension of line #8 with varying ice parameter (left: $h_{ice} = 2\text{ m}$, $\sigma_f = 0.75\text{ MPa}$; middle: $v_{ice} = 0.5\text{ m/s}$, $\sigma_f = 0.75\text{ MPa}$; right: $v_{ice} = 0.5\text{ m/s}$, $h_{ice} = 2\text{ m}$)

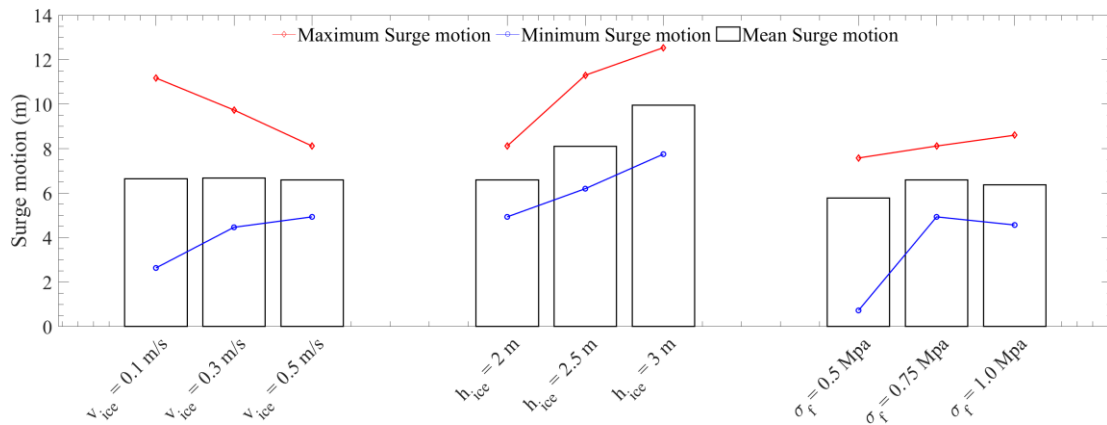


Fig. 14 Statistics of Artic Spar surge motion with varying ice parameter (left: $h_{ice} = 2\text{ m}$, $\sigma_f = 0.75\text{ MPa}$; middle: $v_{ice} = 0.5\text{ m/s}$, $\sigma_f = 0.75\text{ MPa}$; right: $v_{ice} = 0.5\text{ m/s}$, $h_{ice} = 2\text{ m}$)

Table 3 Statistics of mooring top tension of line #8 (unit: MN) (numerical values of Fig. 13)

	v_{ice}			h_{ice}			σ_f		
Max.	3.61	3.52	3.42	3.42	3.65	3.73	3.38	3.42	3.44
Mean	3.33	3.34	3.33	3.33	3.41	3.54	3.30	3.33	3.33
Min.	3.14	3.23	3.25	3.25	3.29	3.40	3.07	3.25	3.23

resonance at that ice speed, as explained in the previous sections. With increasing ice thickness, mooring force is increased, and the platform is drifted farther from the origin. For varying ice flexural strength, the maximum mooring force is slightly increased, while the mean and minimum mooring force do not show any distinct trend.

Finally, the same sets of results for surge and heave motions are given in Figs. 14 and 15. As expected, the general trends of surge motions are very similar to those of mooring tensions given in

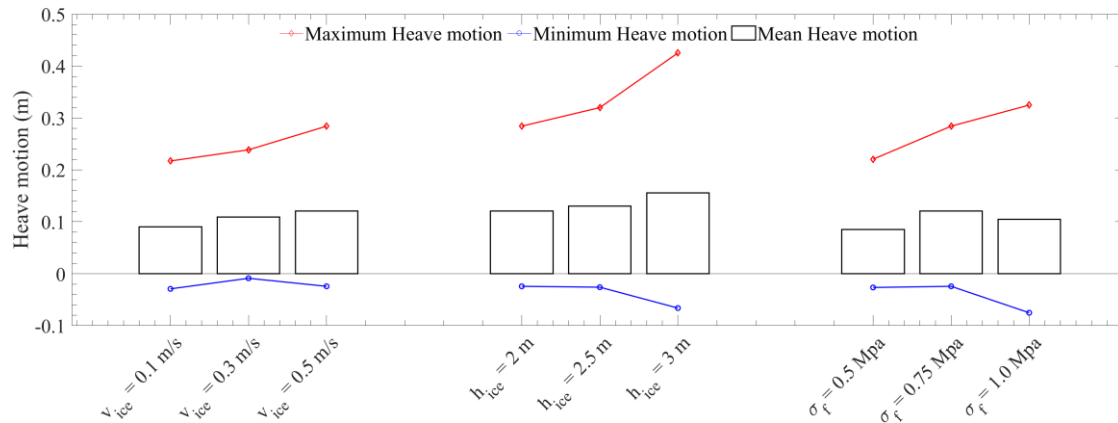


Fig. 15 Statistics of Artic Spar heave motion with varying ice parameter (left: $h_{ice} = 2$ m, $\sigma_f = 0.75$ MPa; middle: $v_{ice} = 0.5$ m/s, $\sigma_f = 0.75$ MPa; right: $v_{ice} = 0.5$ m/s, $h_{ice} = 2$ m)

Fig. 13. In the case of spar heave motion, negative values are of concern since they may cause compressional force on drilling or production risers, which may in turn cause potential buckling (elastic instability) depending on riser types.

5. Conclusions

A series of numerical simulations under various ice conditions were performed for a moored Arctic Spar and the corresponding ice loads and spar motions were assessed. The newly developed ice-floater-mooring fully-coupled-dynamics simulator was used through external coupling between hull-mooring program CHARM3D and DEM program LIGGGHTS based on the named pipe method. The parallel bonding method was employed to model the level ice and its fracture as an assembly of multiple bonded spherical particles. The numerical four-point beam tests were systematically performed to determine the critical bonding strength with given ice properties. Throughout the numerical simulations, the conclusions are made as follows:

- From the visual observation, the sequential processes of dynamic interaction between level ice and Arctic Spar are investigated. When intact ice hits Arctic Spar, it dominantly fails in bending with multiple consecutive breaking. At initial break, the broken ice length is generally 5-10 times the ice thickness, and it becomes 3~5 times the ice thickness due to consecutive breaking. The rubble ice is accumulated in front of and below the the inclined hull and continuously pushes the structure downward and upward to have positive ice forces over entire interaction.
- The time histories of ice forces and surge motions reveal that surge and heave ice forces and spar motions are strongly correlated by having a similar trend of time-series when synchronous resonance happens.
- The 6-DOF structure motions are obtained by the newly developed software in the time domain. Due to the nature of continuous impact-like ice forces, all motions oscillate with respective natural periods. The eccentric loads by asymmetrically broken ices also cause small sway/roll motions and appreciable yaw motions.

- The effect of ice drift velocity on the magnitude of ice force on the floating compliant structure is insignificant, which is different from the case of fixed structures. As the ice drift velocity increases, the ice force signal becomes more random and the force energy is distributed over the wider range of frequency, resulting in smaller Arctic Spar motions.
- Ice thickness significantly affects the magnitude of ice force, showing that both the mean and maximum ice forces are increased with increasing ice thickness.
- When the ice flexural strength increases, the maximum ice force is also increased because high flexural strength makes the bending-mode failure more difficult. However, the mean forces are similar in all cases, which are mainly contributed by rubble-ice accumulation.
- The trends of mooring top tensions are very similar to those of spar surge motions, which means that the mooring tension can be obtained through quasi-static analysis. Small negative heave motions are possible for the spar system with drifting level ice, which may be of concern depending on the types of risers.

Acknowledgments

Authors would like to thank the Center for Computation and Technology (CCT) and LSU High Performance Computing for providing the resources to conduct this research.

References

- Aksnes, V. (2010), "A simplified interaction model for moored ships in level ice", *Cold Reg. Sci. Technol.*, **63**(1), 29-39.
- Barker, A., Timco, G., Gravesen, H. and Vølund, P. (2005), "Ice loading on Danish wind turbines: part 1: dynamic model tests", *Cold Reg. Sci. Technol.*, **41**(1), 1-23.
- Croasdale, K. (1980). Ice forces on fixed rigid structures, Special report 80 80-26, U.S. Army Cold Regions Research and Engineering Laboratory, Hanover
- Croasdale, K. and Cammaert, A. (1994), "An improved method for the calculation of ice loads on sloping structures in first-year ice", *Hydrotech. Constr.*, **28**(3), 174-179.
- Di, S., Xue, Y., Wang, Q. and Bai, X. (2017), "Discrete element simulation of ice loads on narrow conical structures", *Ocean Eng.*, **146**, 282-297.
- Gravesen, H., Sørensen, S. L., Vølund, P., Barker, A. and Timco, G. (2005), "Ice loading on Danish wind turbines: Part 2. Analyses of dynamic model test results", *Cold Reg. Sci. Technol.*, **41**(1), 25-47.
- ISO (2010), ISO 19906:2010 Petroleum and natural gas industries – Arctic offshore structures.
- Jang, H., Kang, H. and Kim, M. (2016), "Numerical simulation of dynamic interactions of an arctic spar with drifting level ice", *Ocean Syst. Eng.*, **6**(4), 345-362.
- Jang, H. and Kim, M. (2021a), "Dynamic ice force estimation on a conical structure by discrete element method", *Int. J. Naval Architect. Ocean Eng.*, **13**, 136-146.
- Jang, H. and Kim, M. (2021b), "Kulluk-shaped arctic floating platform interacting with drifting level ice by discrete element method", *Ocean Eng.*, **236**, 109479.
- Jeon, S. and Kim, Y. (2021), "Numerical simulation of level ice–structure interaction using damage-based erosion model", *Ocean Eng.*, **220**, 108485.
- Ji, S., Di, S. and Liu, S. (2015), "Analysis of ice load on conical structure with discrete element method", *Eng. Comput.*, **32**(4), 1121-1134.
- Jou, O., Celigueta, M.A., Latorre, S., Arrufat, F. and Oñate, E. (2019), "A bonded discrete element method for modeling ship–ice interactions in broken and unbroken sea ice fields", *Comput. Particle Mech.*, **6**(4),

739-765.

- Kloss, C., Goniva, C., Hager, A., Amberger, S. and Pirker, S. (2012), "Models, algorithms and validation for opensource DEM and CFD-DEM", *Progress Comput. Fluid Dy.*, **12**(2-3), 140-152.
- Lavoie, N. (1966), "Ice effects on structures in the northumberland strait crossing", *Ice Pressures Against Structures*, NRC Technical Memo (92).
- Lu, W., Lubbad, R., Høyland, K. and Løset, S. (2014a), "Physical model and theoretical model study of level ice and wide sloping structure interactions", *Cold Reg. Sci. Technol.*, **101**, 40-72.
- Lu, W., Lubbad, R. and Løset, S. (2014b), "Simulating ice-sloping structure interactions with the cohesive element method", *J. Offshore Mech. Arct.*, **136**(3), 031501.
- Mayne, D.C. (2007), "Level ice and rubble actions on offshore conical and sloping structures", Ph.D. Dissertation, University of Calgary, Calgary.
- Nixon, R. and Ettema, R. (1988), Ice Sheet Interaction With a Cable-Moored Platform. University of Iowa IHR report, 148.
- Paavilainen, J., Tuhkuri, J. and Polojärvi, A. (2011), "2D numerical simulations of ice rubble formation process against an inclined structure", *Cold Reg. Sci. Technol.*, **68**(1-2), 20-34.
- Potyondy, D.O. and Cundall, P. (2004), "A bonded-particle model for rock", *Int. J. Rock Mech. Min. Sci.*, **41**(8), 1329-1364.
- Ralston, T.D. (1980), "Plastic limit analysis of sheet ice loads on conical structures", *Phys. Mech. Ice*, 289-308.
- Tian, Y., and Huang, Y. (2013), "The dynamic ice loads on conical structures", *Ocean Eng.*, **59**, 37-46.
- WAMIT, I.N.C. (2006), WAMIT User Manual
- Wang, F., Zou, Z.-J., Zhou, L., Ren, Y.Z. and Wang, S.Q. (2018), "A simulation study on the interaction between sloping marine structure and level ice based on cohesive element model", *Cold Reg. Sci. Technol.*, **149**, 1-15.
- Xu, N., Yue, Q., Bi, X., Tuomo, K. and Zhang, D. (2015), "Experimental study of dynamic conical ice force", *Cold Reg. Sci. Technol.*, **120**, 21-29.
- Yan, Q., Qianjin, Y., Xiangjun, B. and Tuomo, K. (2006), "A random ice force model for narrow conical structures", *Cold Reg. Sci. Technol.*, **45**(3), 148-157.
- Yue, Q., Qu, Y., Bi, X., and Tuomo, K. (2007), "Ice force spectrum on narrow conical structures", *Cold Reg. Sci. Technol.*, **49**(2), 161-169.

PL